Development and comparison of data reconstruction methods for chromotomographic hyperspectral imagers

Michael R. Hawks[*a,b] , Alan Jennings[a], and Ryan Tervo[c]
[a] Air Force Institute of Technology, Wright-Patterson AFB, OH USA 45433; [b] Oak Ridge Institute for Science and Education, 4692 Millennium Drive suite 101, Belcamp, MD USA 21017; [c] 453rd Electronic Warfare Squadron, 102 Hall Blvd, Lackland AFB, TX 78243

ABSTRACT

Chromotomography is a form of hyperspectral imaging that uses a prism to simultaneously record spectral and spatial information, like a slitless spectrometer. The prism is rotated to provide multiple projections of the 3D data cube on the 2D detector array. Tomographic reconstruction methods are then used to estimate the hyperspectral data cube from the projections. This type of system can collect hyperspectral imagery from fast transient events, but suffers from reconstruction artifacts due to the limited-angle problem. Several algorithms have been proposed in the literature to improve reconstruction, including filtered backprojection, projection onto convex sets, subspace constraint, and split-Bregman iteration. Here we present the first direct comparison of multiple methods against a variety of simulatedtargets. Results are compared based on both image quality and spectral accuracy of the reconstruction, where previous literature has emphasized imaging only. In addition, new algorithms and HSI quality metrics are proposed. We find the quality of the results depend strongly on the spatial and spectral content of the scene, and no single algorithm is consistently superior over a broad range of scenes.

Keywords: hyperspectral imaging, tomography, chromotomography, backprojection, projection onto convex sets, split-Bregman method

1. INTRODUCTION

1.1 Background

Hyperspectral imaging (HSI) systems record both the spatial and spectral energy distribution of a scene. Attempting to capture three dimensions of information on a two-dimensional detector array requires some tradeoffs. Conventional HSI systems solve this by removing information from the scene to capture two dimensions at a time, using either spatial (slit) or spectral filters. This creates issues for changing scenes. Conventional systems cannot handle transient or rapidly changing events well. Spectral scanning systems will see the event in at most a few bands, and spatial scanning systems might not even notice the event happened at all.

Tomography estimates an *N*-dimensional structure from a set of *N*-1 dimensional projections. Okamoto [1] and Bulygin [2] were among the first to propose using this idea to reconstruct a three-dimensional hyperspectral data cube from two-dimensional projections, but system modeled here is patterned after Mooney [3]. Chromotomography (CT) systems are similar to slit-less spectrometers in that the entire scene is viewed simultaneously through a dispersive element. This dispersion multiplexes the spatial and spectral information together on the detector. The spectra of different points in an extended scene can overlap, but by rotating the prism one can capture multiple projections which are used to reconstruct the data cube. While this method still requires multiple frames (and therefore time), the instrument captures information from all bands and all spatial points in every frame. This improves situational awareness and provides an ability to measure transient events, as well as boosting instrument throughput.

As will be discussed below, the limited sampling angles available in CT lead to reconstruction artifacts. There are several algorithms that have been developed to address this, generally by applying additional constraints and assumptions. The principle purpose of this paper is to present a side-by-side comparison of the results of each algorithm. Much of the past literature has shown results of one algorithm at a time, using different data. Previous results have shown that CT reconstruction accuracy depends strongly on the content of the scene being imaged [4] [5], so direct comparison has not been possible based on previously published results. In addition to this comparison, several new reconstruction ideas were also tried, and will be presented below.

2. THEORY

2.1 Projections

For an object represented by the hyperspectral data cube, $f(x,y,\lambda)$, the CT instrument measures projections in which each wavelength layer of the f has been sheared laterally by a wavelength-dependent distance. We generally represent the set of all projections as another 3-D array, g. Using the vector $\mathbf{x}$ to represent the 2 spatial dimension of the image, the image (projection) recorded at prism angle θ_m is

$$g_m(\mathbf{x}) = g(\mathbf{x},\theta_m) = \sum_{n=1}^{N} f(\mathbf{x} - \mathbf{p}_m d_n, \lambda_n) . \tag{1}$$

Here $n \in \{1,2,...N\}$ is the band number, d_n is the scalar shift distance at wavelength λ_n, and $\mathbf{p}_m = (\cos\theta_m, \sin\theta_m)^T$ is the shift direction for the prism orientation during the m^{th} frame. The projections are really an integral over wavelength, but for convenience we use a sum over the discrete resolvable wavelength bins to approximate the continuous spectrum.

Notice the shift imparted by the prism can also be thought of as a convolution by an off-center point-spread function. In the Fourier transform space this becomes multiplication by a complex phase, so we can then rewrite equation (1) as

$$G_m(\mathbf{u}) = \sum_n F_n(\mathbf{u}) \exp\left[-2\pi i \left(\mathbf{u}\cdot\mathbf{p}_m d_n\right)\right] . \tag{2}$$

Here we use capital letters to denote the Fourier transforms and $\mathbf{u}$ for the two-dimensional spatial frequencies.

Following Brodzik's notation [6], we can represent equation (2) as the matrix operation,

$$\begin{pmatrix} G_1(\mathbf{u}) \\ \vdots \\ G_M(\mathbf{u}) \end{pmatrix} = A(\mathbf{u}) \begin{pmatrix} F_1(\mathbf{u}) \\ \vdots \\ F_N(\mathbf{u}) \end{pmatrix} \tag{3}$$

where the elements of the $M \times N$ matrix A are given by

$$A_{mn}(\mathbf{u}) = \exp\left[-2\pi i \left(\mathbf{u}\cdot\mathbf{p}_m d_m\right)\right] \tag{4}$$

The argument $\mathbf{u}$ is used above as an explicit reminder that each matrix A is specific to a particular spatial frequency, so that equation (3) must be repeated for each $\mathbf{u}$. We will drop that argument for brevity, so we rewrite equation (3) as

$$G = AF . \tag{5}$$

2.2 Backprojection

Backprojection, or the inverse Radon transform, is the most straightforward method to construct an estimated hypercube, $f_e(\mathbf{x},\lambda_n)$. There are several ways to implement back-projection. The simplest conceptually is to shift the projections back by a distance opposite to the shift imparted by the prism. The shifted projections, $g'_m(\mathbf{x}) = g_m(\mathbf{x} + \mathbf{p}_m d_n)$, are summed over all prism angles [7]. Because the distance d_n is wavelength dependent [8], this is done separately for each reconstructed wavelength. Consider the sum represented by backprojection:

$$f_e(\mathbf{x},\lambda_n) = \frac{1}{MN} \sum_{m=1}^{M} g_m(\mathbf{x} + \mathbf{p}_m d_n) . \tag{6}$$

Because each g_m represents a sum over all wavelengths, this shows that every wavelength in the reconstruction contains energy from every wavelength of the object, which leads to spatial and spectral artifacts.

The more compact notation is to solve this in the Fourier domain via

$$F_e = A^{-1} G . \tag{7}$$

Examination of A shows it is rank-deficient for most spatial frequencies, so the Moore-Penrose pseudo-inverse, A^+, would in general be preferred.

Unfortunately, the system transfer matrix, A, has a large conical null-space, sometimes referred to as the cone of missing information (see [6] for a more detailed discussion). Thus equation (7) does not have a unique solution, even in the limit of noise-free data. In this case, all reconstruction artifacts are contained within the null space of A. The remaining reconstruction algorithms beyond back-projection are all attempts to use other constraints to deal with this issue.

2.3 Algorithms

A number of algorithms from the literature have been implemented here. We will briefly summarize each, but the reader is referred to the original papers for more detail.

1. Backprojection (BPrj): as described above, this can be done using either the shift-and-add method of equation (6) or the Fourier method of equation (7). In practice we find the both methods agree within the significant digits, but the Fourier method is simpler to code as it avoids the extra step of interpolating after shifting images by fractions of a pixel.

2. Backprojection then filtering (BPF): Deming [9] demonstrates a form of Tikhonov regularization that is equivalent to the conventional filtered back projection [10], but more appropriate for the sampling space of a rotating prism system. In this method, the filtered object estimate F_e' is computed from the backprojection estimate F_e by

$$\mathcal{F}_\lambda\left(F_e'\right) = \frac{\mathcal{F}_\lambda\left(F_e\right)}{\mu + \mathcal{F}_\lambda\left(B\right)} \tag{8}$$

   where μ is the regularization parameter, $B = 2\pi J_0(2\pi d\,\mathbf{u}\lambda)$, and J_0 is the zero-order Bessel function. The $\mathcal{F}_\lambda$ in equation (8) indicates a Fourier transform in the spectral dimension.

3. Projection onto convex sets (POCS): this is an iterative approach that applies additional constraints to infer reasonable information to fill in the null space of A. In Brodzik's approach [6], the known image content from within the range of A is referred to as the transform-domain constraint. The object-domain constraint is based on observing that pixel spectra in hyperspectral images of real scenes tend to be correlated. This is enforced by using singular value decomposition (SVD) to project the spectra onto a basis set of the first K eigenspectra (with $K \ll N$). As implemented here, K is automatically chosen to use the singular values that explain 99% of the variation.

4. Subspace constraint algorithm (SCA): An [11] presents another way to apply the same conceptual constraints used in POCS. Here, equation (7) to find a direct solution, which is only retained in the region where A is full rank and the projections are adequately sampled. The remainder of the transform-space data cube is filled in by again using SVD to limit the number of eigenspectra & eigenimages to use.

5. Split-Bregman iteration (SBI): the above algorithms amount to different computational methods to find a least-squared-error solution, or the solution that minimizes the L^2-norm error term,

$$\left\|AF - G\right\|_2^2 \ . \tag{9}$$

   If we instead seek to minimize the L^1 norm error, we can take advantage of some very fast algorithms [12, 13]. The L^1 norm in this context is generally used as a numerically-stable proxy for the L^0 norm, so in minimizing this we are effectively imposing a sparsity constraint. Cooke [14] also demonstrated a highly efficient variant of this for the special case of only 8 projections.

6. Deconvolution (DCnv): backprojection gives rise to circular artifacts, where the radius of the circle is determined by the difference between the reconstruction wavelength and the source wavelength [4]. In three dimensions, this is a conic point spread function. Here, we use the Richardson-Lucy iterative deconvolution method [15] to attempt to remove artifacts. The point spread function was estimated based on the backprojection of a broadband point source.

7. Algebraic reconstruction technique (ART): this is an iterative method in which equation (1) is applied to the estimated object to compute what Colsher calls raysums, $r_m(\mathbf{x})$ [16],

$$r_m(\mathbf{x}) = \sum_{n=1}^{N} f_e(\mathbf{x} - \mathbf{p}_m d_n, \lambda_n) \tag{10}$$

   These are, in effect simulated projections of what the system would measure if our estimate, f_e, were the true object. These are compared to the measured projections to create the error estimate $E(\mathbf{x}) = g(\mathbf{x}) - r(\mathbf{x})$. Because this error could come from anywhere in the cube, it is uniformly back-projected to create a new object estimate,

$$f_e^{(k+1)} = f_e^k + \frac{1}{M}\sum_{m=1}^{M} E_m(\mathbf{x} + \mathbf{p}_m d_n) \tag{11}$$

where k is the iteration number.

8. Modified ART (MART): we propose an approach that, like ART, begins by comparing g to r. In this modification, we apply a correction after each wavelength image is computed, rather than computing the entire cube. The reasoning behind this is as follows. Imagine the scene contains a number of monochromatic objects at distinct wavelength. The light from each object creates artifacts in all images except the one wavelength where the image belongs. If we had some method to decide which image was correct, we could then forward project that image to estimate the object's contribution to g, and then remove it before continuing on to other wavelengths. This method is repeated until the energy remaining in g is below a user-selected threshold (5% of the original energy, in the results shown below). The mathematical expression of this looks much like ART, except we now have an opportunity to apply some logic to localize the error sources. For the results presented here, we simply go through each band in order, but there are other options.

9. Extreme-value reconstruction (EVR): this is a class of nonlinear methods rather than a specific algorithm. The version proposed here is based on the observation that reconstruction artifacts are always additive. Consider a single pixel in the backprojected image. If the pixel value is zero for any prism angle, then we assume its correct value is zero, and any non-zero values are due to off-wavelength artifacts. More generally, we take the back-projected pixel value that is the minimum over all angles,

$$f_e(\mathbf{x}, \lambda_n) = \min_{\theta}\left(g_m(\mathbf{x} + \mathbf{p}d_n)\right) \tag{12}$$

10. Constrained backprojection (CBP): Back-projection is based on a sum of shifted images. Image data that has been shifted by the correct distance (because our reconstruction wavelength is in-band to the source) will appear stationary with respect to prism angle. We propose a technique that rejects backprojections on a pixel-by-pixel basis if the change in intensity with respect to prism angle exceeds some user-defined threshold. For similar reasons, any pixel (after summing) with a value less than $M \times$ threshold is also rejected.

11. Hybrid constraint: Lastly, we note that some algorithms tend to produce better image quality, while others are better at preserving spectral accuracy. The hybrid method uses the panchromatic image (summed over all wavelengths) from one reconstruction as a constraint to renormalize the spectra produced by a different reconstruction. For the results shown below, the hybrid algorithm automatically selected the best results of the previous algorithms to use.

3. METHODOLOGY

3.1 Simulated data

Object data cubes were simulated to facilitate quantitative comparison of processed results against a known "truth" target cube. The details of each data cube are described below.

1. A high-contrast synthetic bar target: this is a 64×64×64 sparse cube with the following objects embedded in a dark field: (a) a broad-band point source located at image center from bands 2-20; (b) a monochromatic 3-bar pattern in band 24, located NW of center; (c) a monochromatic 8x8 pixel square in band 31 at image center; and (d) a narrow-band 3-bar pattern in bands 42-48, located SE of center. These objects, shown in Figure 1, were chosen to create high-contrast and high spatial frequencies with a variety of spatial extent and bandwidth.

2. 3-D Shepp-Logan head phantom (as implemented by Schabel [17]). Here we use the third dimension, usually interpreted as depth, as a surrogate for wavelength. A 64×64×64 cube was simulated, then zero-padded (to simulate the field stop) out to 128×128×64. Sample images from this cube are shown in Figure 2.

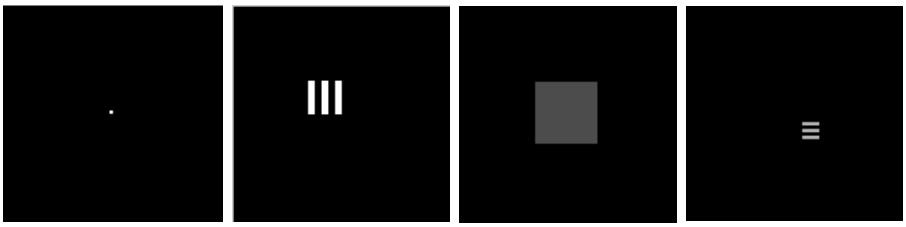

(a) (b) (c) (d)

Figure 1: four single-band images from the object cube 1 to show the primitive objects.

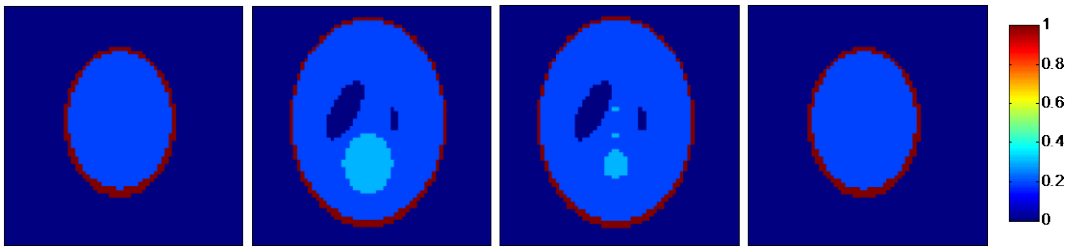

Figure 2: image slices from the modified 3D Shepp-Logan head phantom. As used here, each slice represents an image in a single wavelength band.

3. AVIRIS data cube from Cuprite, NV (from 14 Oct, 2010). The full file was cropped down to 100×100 spatial pixels and 31 spectral bands covering the visible spectrum. This was zero-padded to 200x200 spatial pixels to simulate the effects of the field stop. A small bright spot simulating steady combustion flame was digitally added in order to have a region of high spatial and spectral contrast included in the scene. This was modeled as a circle with a radius of 1.6 pixels. The fireball spectrum is based on a 3,000K blackbody, with a few atomic emission lines added to provide spectral features. Images from the scene and a panchromatic image of the extracted cube are shown in Figure 3.

(a)

(b)

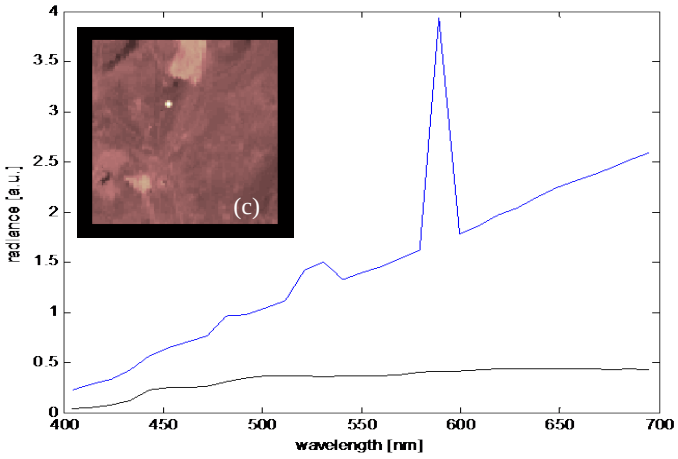

(d)

Figure 3: (a) pseudo-color image constructed from the AVIRIS data cube from Cuprite, NV. (b) a closer view of the area shown in the yellow box of panel a. (c) false color panchromatic image from object cube extracted from the region of the yellow box in panel b. (d) simulated flame spectrum (blue line) added to create the bright spot in panel (c), along with the mean spectrum of the background (black line).

After creating the object cubes, each was forward projected using equation (5) to simulate the effects of an idealized CT instrument (i.e. no detector noise, no aberrations, no motion blur, etc.). The same set of simulated measurements were then used as input to all reconstruction methods.

Some methods, such as projection onto convex sets, require an estimated object cube as a starting point for iteration. The results from back-projection according to equation (7) were use as the starting point for all such cases. Some experiments were conducted to see if there was any significant benefit to using other reconstruction methods to generate this input, but initial results showed no clear advantage to this. For example, using the results of split-Bregman iteration as an input to the subspace constraint algorithm did cut the image error nearly in half, but raised the mean spectral angle by nearly a factor of 3.

3.2 Quantifying results

The example above points out another issue: how to best characterize the quality of the reconstruction results. There are a number of metrics to characterize image quality or spectral accuracy, but the community has not adopted a metric that addresses the combination of the two.

A number of image quality metrics were tested, but the results presented here all use the structural similarity index (SSI) proposed by Wang [18], as implemented by the SSIM function in Matlab's Image Processing Toolbox. SSI compares two images--in this case two single-wavelength image slices taken from the original object cube and the reconstructed estimate. Values of SSI can range from 0 to 1, with 1 indicating identical images. SSI was chosen as a metric because it considers not only image brightness, but also contrast and structure. It is therefore a good indicator of how recognizable an image would look to a human operator. One drawback to this metric is that it does not handle dark images well because of the normalization method. For example, the low and high wavelength extremes of the 3D head phantom have no objects. Here reconstructed images that contain any energy at all report poor SSI.

Spectral accuracy is characterized using the spectral angle, *SA*, which is a measure of the overlap of two vectors,

$$SA = \arccos\left(\frac{\vec{a}\cdot\vec{b}}{|\vec{a}||\vec{b}|}\right) . \tag{13}$$

Here $\vec{a}$ represents the true spectrum for one pixel of the object and $\vec{b}$ is the reconstructed spectrum of the same pixel. Identical spectra produce a spectral angle of 0, while orthogonal spectra give $SA = \pi/2$. In practice, we add a small value (equal to the least significant digit) to both numerator and denominator to avoid divide-by-zero issues in dark pixels.

We have metrics for image quality and for spectral accuracy. For purposes of comparison, we propose a quality metric, *Q*, that combines the spectral angle (averaged over all spatial pixels) and the image quality (averaged over all bands). If the number of pixels in each image is $p \times p$, we define quality as

$$Q = \frac{1}{Np^2}\sum_{\mathbf{x}} SA(\mathbf{x}) \cdot \sum_{n}\left(1 - SSI(\lambda_n)\right) . \tag{14}$$

Note that we use (1-*SSI*) so that lower scores indicate better performance as with spectral angle. This metric assumes that imagery and spectra are of equal importance, so for some applications it may be more appropriate to construct a combined metric that includes relative weighting functions.

When computing these metrics, we first renormalize the entire data cube to the range [0,1] and crop the reconstruction to remove the field stop region of zero padding in the object.

4. RESULTS

4.1 Parameter selection

Several of the algorithms have user-selected parameters. Values for these were chosen by comparing the quality of the results as a function of filter parameter, as shown in Figure 4. We assume the optimal value will not be known in general, so there was no attempt to optimize -- rather, we selected a value that seemed to offer relatively good and stable performance over the range of targets used in this study.

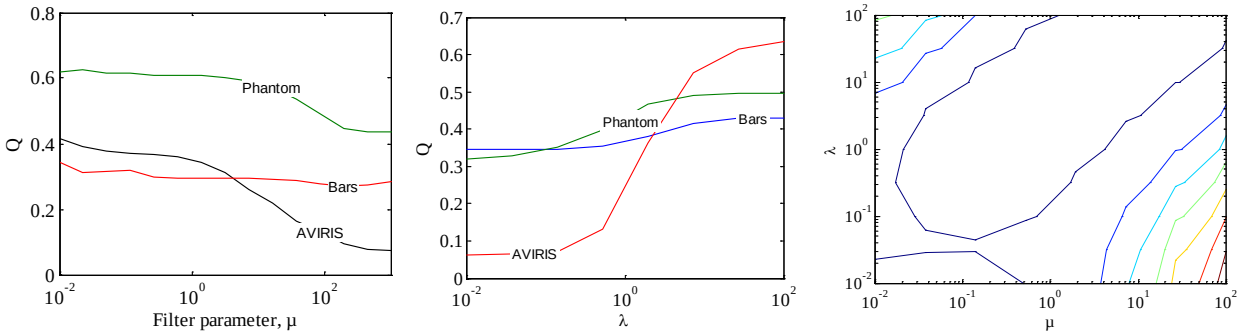

Figure 4: Parameter selection plots. (a) quality as a function of filter parameter for BPF, compared for all targets. (b) quality as a function of splitting parameter for SCA. (c) contour plot of quality in SBI results after 3 iterations for the head phantom target (blue = best to red = worst).

Table 1: Parameter values used in this study. See references for detail on parameter definitions

Algorithm	Parameter	Value	Algorithm	Parameter	Value
BPF [9]	μ - regularization coeff.	100	POCS [6]	N - # of iterations L - singular value threshold	10 0.99
SCA [11]	λ - Splitting coefficient	0.1	SBI [18]	μ - regularization const. λ - Splitting coefficient N - # of iterations	0.5 2 10
ART [19]	N - # of iterations	10	MART	N - # of iterations	10

4.2 Image quality

Figure 4 shows example single-wavelength images from different reconstructions of the bar target. Each row of images are for the same wavelength, and each column are from the same reconstruction method (or from the original object, in the far left column). For brevity, not all algorithms or wavelengths are shown here. These images demonstrate the off-wavelength artifacts. Most reconstruction methods recover the shape of the bright objects fairly well, but struggle to produce the correct brightness and fail in the dark region of the images.

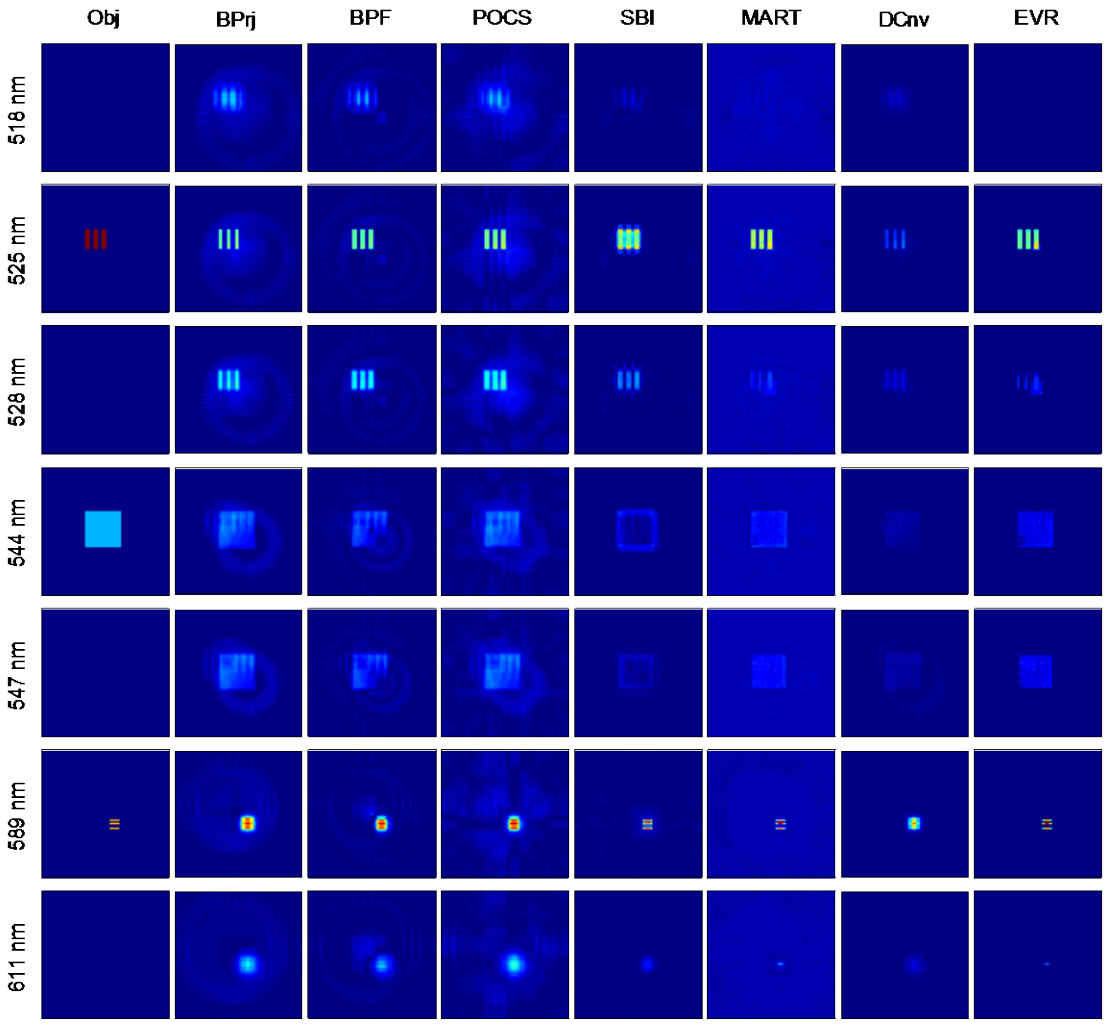

Figure 5: false-color single-wavelength images from the original object and five different reconstructions of the bar target. Each row shows images for the same wavelength, and each column shows images from the same reconstruction method. The color scale is the same for all images, with blue for low intensity and red for high.

Figure 5 demonstrated that image quality is not uniform with respect to wavelength. Figure 6 shows plots of the Structural Similarity Index (SSI), as a function of wavelength for the head phantom target and the AVIRIS target. Figure 7 shows image quality for panchromatic images created by summing each reconstruction over all bands.

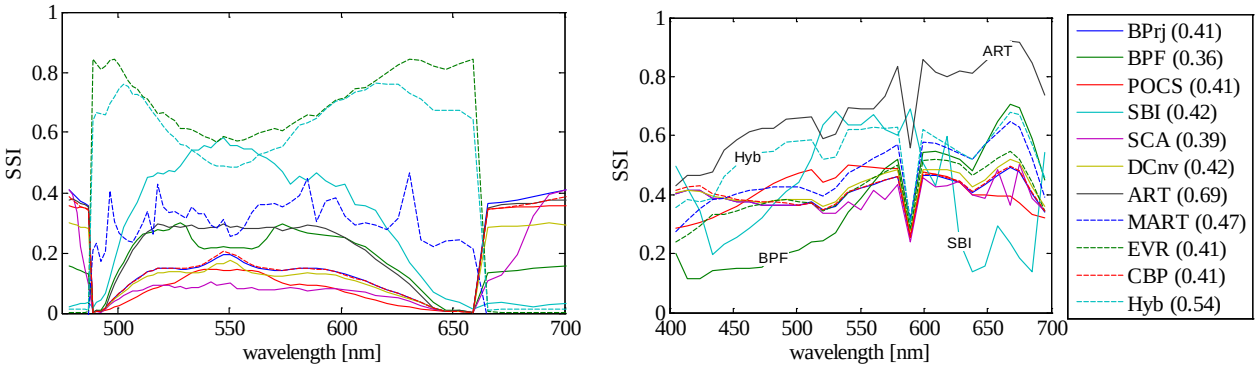

Figure 6: Structured Similarity Index as a function of spectral band for all reconstructions of the 3D phantom (left) and AVIRIS data (right). The spectrally-averaged SSI from AVIRIS reconstructions are shown in parenthesis in the legend. Notice the SSI changes sharply in regions of sharp spectral features, such as the Na emission line of the simulated fireball.

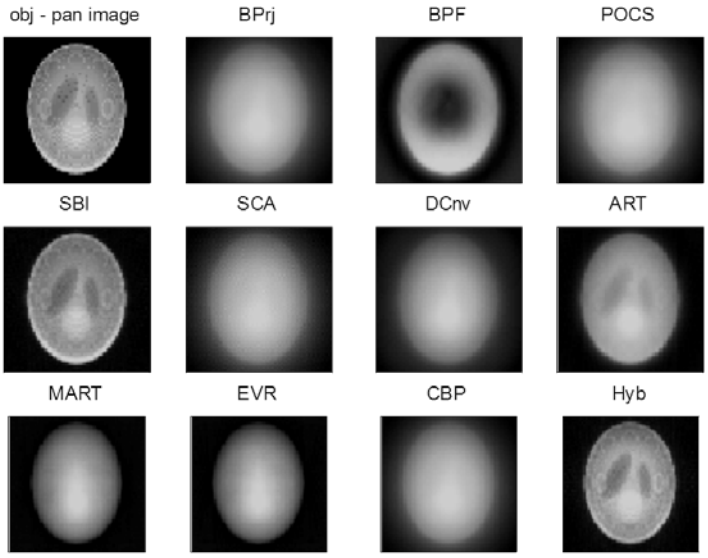

Figure 7: Panchromatic images from 11 CT reconstructions of the head phantom target.

4.3 Spectral Accuracy

The primary way to compare spectral accuracy is through the spectral angle. Figures 8 and 9 show images of the spectral angle at each spatial pixel for all reconstructions of the head phantom target and the AVIRIS target. The numbers in parentheses above each image show the spatial average, in radians.

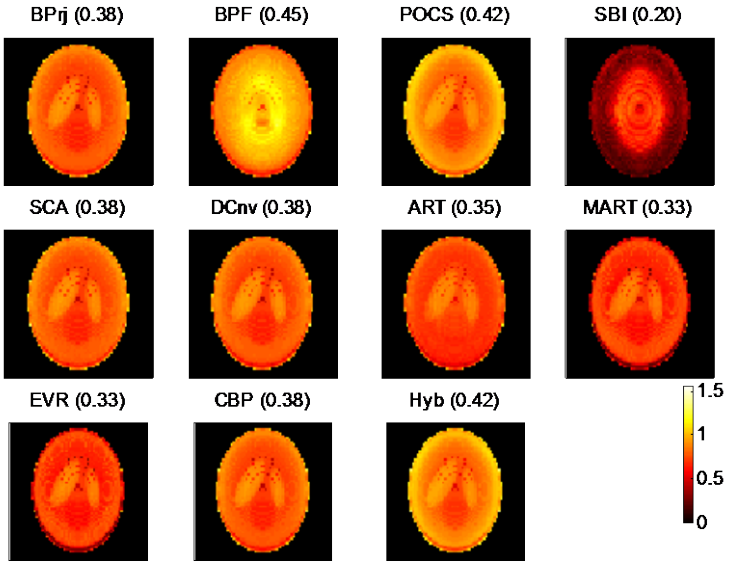

Figure 8: Spectral angles in radians for all reconstructions of the 3D Shepp-Logan phantom. Spatially-averaged spectral angle is shown in parentheses above each image.

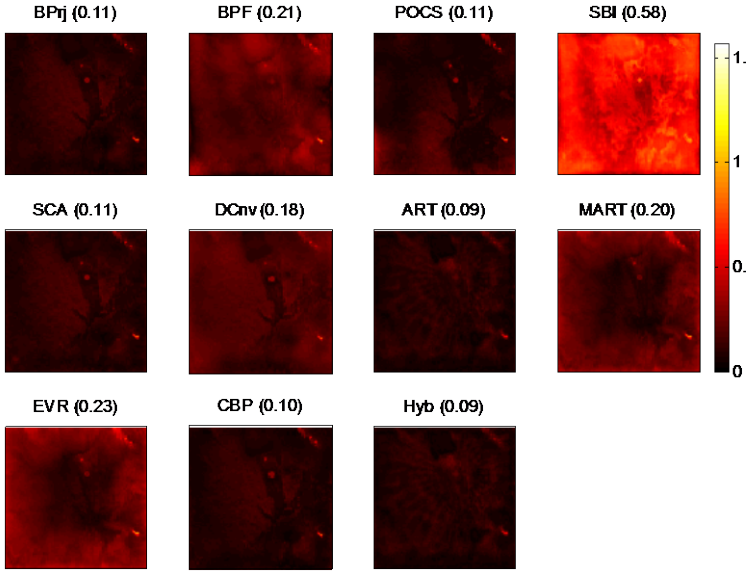

Figure 9: Spectral angle for each reconstruction of the AVIRIS data, in radians. The number in parentheses above each plot shows the spatially-averaged spectral angle. Note that the methods with the best SSIM in Figure 6 have the worst spectral angle.

4.4 Combined HSI quality metric

Figures 10 and 11 show how the image quality and spectral accuracy combine into the overall scores, which are then compared for all targets. In figure Figure 10, both spectrally-averaged SSI and spatially-averaged spectral angle are plotted for each algorithm. The values are overlaid on contours of constant Q, with lower values (dark blue) indicating best performance. In each plot there is a tight grouping of points near the "BPrj" backprojection result. This grouping includes the unlabeled points for SCA and CBP for all targets. The group also includes unlabeled points for BPF and POCS in the bar target; DCnv in the phantom; and POCS in the AVIRIS data. For the AVIRIS data, the SBI result is

off-scale (mean *SSI* = 0.42, mean *SA* = 0.58). There are few consistent trends in these results across different target sets. There is a weak negative correlation between image quality and spectral accuracy, for example.

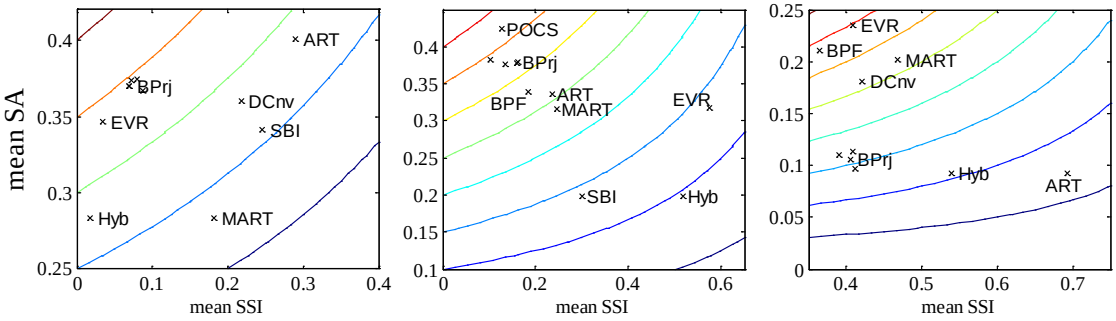

Figure 10: Results for reconstructions of the bar target (left), head phantom target (center) and AVIRIS target (right). Lines show contours of constant *Q* (from blue = best to red = worst).

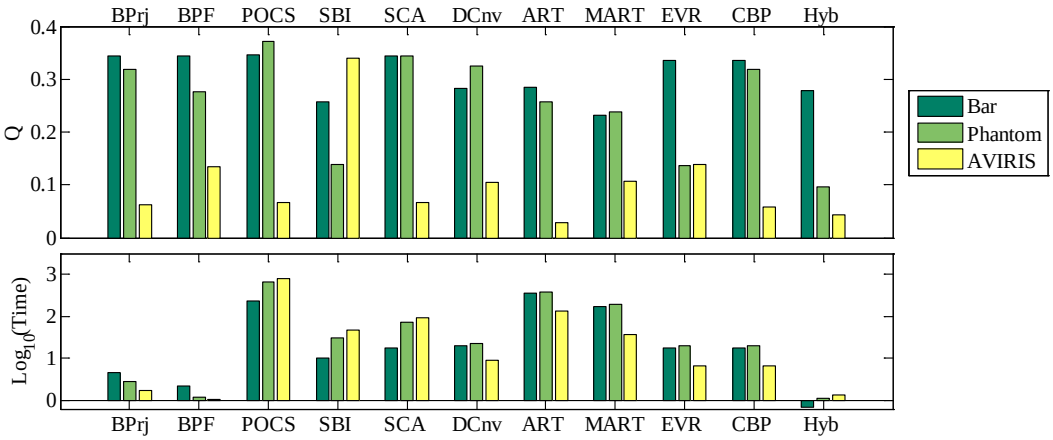

Figure 11: combined HSI quality metric, *Q*, and computation time (Log[*T*, in seconds]) for all cases. Each bar group is for one algorithm; each bar color is for one target.

Actual computation times compound in most cases, because many algorithms rely on a first estimate from backprojection as input. Figure 11 does not take this into account. For example, Figure 11 seems to indicated backprojection then filtering (BPF) is the fastest method. This figure only shows the time taken for the filtering step after backprojection. This is done because the initial estimate could be generated by any algorithm before filtering.

5. CONCLUSIONS

The results shown here that the quality of CT reconstruction depends strongly on the content of the target. Here we tested 11 reconstruction algorithms against two high-contrast synthetic targets and one synthesized from actual HSI data. The results vary significantly from one target to the next. The common trend over these targets was the Hybrid algorithm and modified-ART algorithms tend to perform well for all targets. The split-Bregman iteration performs very well on the bar target but poorly on AVIRIS data, which is to be expected since the method assumes sparsity. Surprisingly, the Hybrid method, which is based on a relatively weak assumption, also tends to perform well. Results of the other algorithms were inconsistent.

The fastest method (as implemented in our code) is backprojection, with POCS being the slowest. Filtering after backprojection can be done very quickly, but adds little value and sometimes even degrades the quality of the reconstruction.

Future work will further investigate methods to evaluate the accuracy of reconstructions for the case of an unknown target.

ACKNOWLEDGMENTS

The views expressed in this paper are those of the authors and do not necessarily reflect the official policy of the U.S. Air Force, the Department of Defense, or the U.S. Government.

WORKS CITED

[1] T. Okamoto and I. Yamoguchi, "Simultaneous acquisition of spectral image information," *Opt. Lett,* vol. 16, no. 16, pp. 1277-1279, 1991.

[2] F. V. Bulygin, G. N. Vishnyakov, G. G. Levin and D. V. Karpukhin, "Spectrotomography--a new method of obtaining spectrograms of 2-D objects," *Opt. Spectrosc. (USSR),* vol. 71, no. 6, pp. 561-563, Dec 1991.

[3] J. Mooney, V. Vickers, M. An and A. Brodzik, "High-throughput hyperspectral infrared camera," *JOSA-A,* vol. 14, no. 11, pp. 2951-2962, 1997.

[4] K. J. Dufaud, M. R. Hawks and R. Tervo, "Experimental characterization of the quality of image reconstruction from a chromotomographic system," in *Proc of the SPIE,* 2014.

[5] R. Tervo, M. Hawks, G. P. Perram and M. Fickus, "Effects of optical aberration on chromotomographic image reconstruction," in *Proc of SPIE,* 2014.

[6] A. K. Brodzik and J. M. mooney, "Convex projections algorithm for restoration of limited-angle chromotomographic images," *J. Opt. Soc. Am. A,* vol. 16, no. 2, pp. 246-257, 1999.

[7] J. T. Dobbins III and D. J. Godfrey, "Digital x-ray tomosynthesis: current state of the art and clinical potential," *Phys Med Bio,* vol. 48, pp. R65-R106, 2003.

[8] C. Su'e, "Characterization of a hyperspectral chromotomographic imaging ground system," Air Force Institute of Technology, WPAFB, OH, M.S. Thesis ADA557752 (2012).

[9] R. Deming, "Chromotomography for a rotating-prism instrument using backprojection, then filtering," *Opt Lett,* vol. 31, no. 15, pp. 2281-2283, Aug 2006.

[10] J. Hsieh, "Computed Tomography, 2ed.," SPIE Press, Bellingham, WA, 2009.

[11] M. An, A. Brodzik, J. Mooney and R. Tolimieri, "Data restoration in chromo-tomographic hyperspectral imaging," *Proc. of SPIE,* vol. 4123, pp. 150-161, 2000.

[12] T. Goldstein and S. Osher, "The split-Bregman method for L1-regularization problems," *SIAM J. Imaging Sci,* vol. 2, no. 2, pp. 323-343, 2009.

[13] A. Szlam, Z. Guo and S. Osher, "A split Bregman method for non-negative sparsity penalized least squares with applications to hyperspectral demixing," in *Proc of IEEE Conf Image Proc*, Hong Kong, 2010.

[14] D. J. Cooke, "A Discrete X-ray transform for chromotomographic hyperspectral imaging," Air Force Institute of Technology, Wright-Patterson AFB, M.S. Thesis ADA576040 (2013).

[15] D. Biggs, "Acceleration of Iterative Image Restoration Algorithms," *App Opt,* vol. 36, no. 8, pp. 1766-1775, 1997.

[16] M. Schabel, "3D Shepp-Logan Phantom," 20 12 2005. [Online]. Available: http://www.mathworks.com/matlabcentral/fileexchange/9416-3d-shepp-logan-phantom. [Accessed 19 02 2015].

[17] Z. Wang, A. C. Bovik, H. R. Sheikh and E. P. Simoncelli, "Image quality assessment from error visibility to structural similariy," *IEEE Trans Im Proc,* vol. 13, no. 4, pp. 600-612, April 2004.

[18] J. Gilles, October 2011. [Online]. Available: http://framelet-mri.googlecode.com/hg-history/bfc2d161d19c87938438368392dd2529b261ee9b/BregmanCookbook/BregmanCookbook.pdf.

[19] J. G. Colsher, "Iterative three-dimensional image reconstruction from tomographic projections," *Comput Graph Imag Proc,* vol. 6, pp. 513-537, 1977.